

HiSST: 4th International Conference on High-Speed Vehicle Science & Technology

22-26 September 2025, Tours, France



Mach 5 Turbojet-Ramjet Vehicle Trajectory Feasibility Analysis

David J. Cerantola, Pradeep Dass2

Abstract

Designing spacecraft for missions with wide velocity ranges is a challenging task given the monumental performance variations between subsonic and hypersonic. A trajectory analysis is a beneficial exercise early in the design process to help identify the critical operating conditions needed for component design. Existing publicly available trajectory evaluation tools do not have the functionality to trim the aircraft, quantify static margin, or have the necessary degrees of freedom to satisfy the performance needs. With few exceptions, the emphasis of existing trajectory analyses is on optimized solutions; however, developing a satisfactory performance coefficient data-set for a multi-phase cruise vehicle to yield feasible solutions is not obvious. This paper evaluates a trajectory for a turbo-ramjet spacecraft from a horizontal take-off to a Mach 5 at 30 km altitude mission objective and descent to a horizontal landing where the initial performance dataset is insufficient to find a solution. Trajectories were evaluated using the Dymos library built onto OpenMDAO where input lift, drag, and moment coefficients were obtained from CFD and thrust and fuel consumption coefficients from pyCycle. The methodology section introduces a trimming module and solver strategy that leverages specific excess power to advise an initial guess. The obtained trajectory with a minimize time objective shows the trimmed vehicle travelled 672 km in 872s, had longitudinal static stability, and required 11.6% of take-off mass to be fuel. A 20% thrust enhancement factor applied to the ramjet phase was necessary to achieve 30km altitude whereas 28km altitude was achieved without enhancement.

Keywords: Trajectory, MDO, turbojet, ramjet, feasibility

Nomenclature

Latin

 a_x – horizontal acceleration, m/s² a_z – vertical acceleration, m/s²

 C_D – drag coefficient C_L – lift coefficient

 C_m – longitudinal moment coefficient C_T – thrust coefficient

CIT - compressor inlet temperature, K

D – drag, N

g – gravity constant, m/s²

GD - glide descent phase

h – altitude, m

 I_{sp} — specific impulse, s L — lift, N

M – Mach number

m – mass, kg mix - mix phase

PL – powered descent phase

q – freestream dynamic pressure, Pa (psi)

r - range, m

RJ - ramjet phase

 $S\,$ – reference area, m^2

SEP - specific excess power, m/s

SET – specific excess thrust

t – time, s

TJ - turbojet phase

v - velocity, m/s

 W_{tot} – vehicle weight, N

Greek

 α – angle-of-attack, deg

 δ – elevator deflection, deg

 γ – flight path angle, deg

Subscripts

H2 - hydrogen

jetA - liquid hydrocarbon fuel

¹Space Engine Systems, Edmonton, Canada, T6R 3L6, dcerantola@spaceenginesystems.com ²Space Engine Systems, Edmonton, Canada, T6R 3L6

1. Introduction

Numerous entities have recently expressed interest in developing hypersonic technologies. Applications include military, orbital launchers with reusable components or the next generation of civilian aircraft. In response, the ambition for the AIAA CFD 2030 vision shared at SciTech 2025 are validated hypersonic models over a trajectory for cruise and glide vehicles. Although many multidisciplinary design and optimization (MDO) studies have identified trajectory solutions [1–4], few have remarked about the feasibility challenges associated with the path constraints [4, 5], the impact of trimming [6], respecting thermal limits including maximum turbojet (TJ) compressor inlet temperature, or accounting for additional degrees-of-freedom via control surfaces that make flight possible. Even fewer efforts for cruise vehicles have involved multiple propulsion phases.

An airbreathing spacecraft with a mission objective including significant changes in altitude and velocity remains a formidable proposal due to the technological and engineering challenges associated with the engines, thermal protection systems, and control systems [1]. Inlets and nozzles either require moving parts or off-design performance penalties need to be offset with excess thrust. For combined-cycles utilizing a TJ, extending TJ operation to at least Mach 3 is a favourable decision to mitigate ramjet (RJ) thrust deficit at lower Mach given the insight into using precoolers [7–11]. Precoolers alleviate working difficulties for rotating parts exposed to high Mach flow temperatures and can improve performance since the temperature drop effect is greater than the negative impact of total pressure loss associated with the heat exchanger resistance [10]. At higher Mach, stability is more difficult to sustain due to reduced aerodynamic control power and damping [12, 13]. Developing a dataset over the flight envelope where thrust exceeds drag and lift equals weight at the required altitude is not obvious. Consequently, trajectory optimization may never lead to a feasible outcome.

Control theory techniques that obey imposed constraints are typically used to calculate and optimize time-variant dynamic-system trajectories with little prior knowledge [1]. The control problem is discretized using direct methods whereby a sequential quadratic programming solver is applied to the transformed nonlinear programming problem (NLP). Solvers exist that deal with large, sparse NLP where Interior Point OPTimizer (IPOPT) is better equipped to handle linkages between propulsion phases. Collocation methods offer a robust approach to segment the time history and have proven successful in efficiently converging while maintaining solution stability. A higher accuracy collocation approach uses polynomials to approximate the state and control functions where both Radau Pseudospectral method [14] and Gauss-Lobatto Quadrature [15] have been implemented successfully in spacecraft trajectory optimization. At each iteration, solutions are evaluated for feasibility and optimality of the objective function. The process is terminated either when the specified tolerance or a predefined number of iterations is reached.

The purpose of this paper is to obtain a trajectory solution using the Dymos library built onto OpenMDAO for a horizontal take-off and landing reusable airbreathing engine spacecraft employing a combined-cycle turbojet-ramjet propulsion system with a Mach 5 maximum velocity at 30 km altitude mission objective. Whereas similar publications focus on obtaining an optimized solution, this paper articulates the importance of a good initial guess, constructing an adequate performance dataset, and solver strategy towards achieving a feasible solution. Obtaining a trajectory result early in the design process is beneficial to appreciate the diversity of needs during the various stages of flight and advise on degrees of freedom needed to obtain a solution. Noteworthy contributions from this effort include the presentation of results for a trimmed cruise vehicle with multiple propulsion phases that has longitudinal static stability throughout the mission and respecting structural and flight dynamics constraints.

Section 2 outlines the problem setup whereby the Dymos trajectory tool implements the flat-Earth assumption and solves the 2D governing equations for range and height. Thrust and fuel consumption coefficients are obtained from the 1D pyCycle engine cycle tool whereas lift, drag, and longitudinal moment coefficients are obtained using 3D steady-RANS solutions at points-in-the-sky. Factors are applied to the thrust and/or drag coefficients using an iterative approach of identifying constraint violations in trajectory attempts. Section 3 shares a solution satisfying the mission objective and Sec. 4 lists the conclusions.



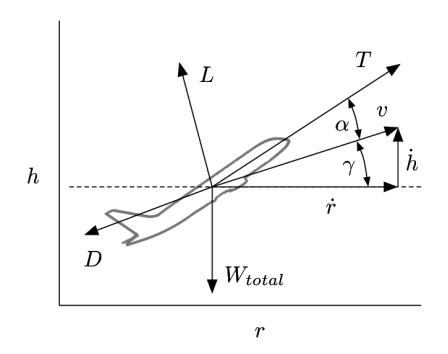


Fig 1. Space Engine Systems Hello-1X airbreathing spacecraft.

Fig 2. Free-body diagram for a commercial aircraft on a planar flight path, from [17]

Table 1. Trajectory study definition.

mission requirement	ground take-off, accelerate and ascend to Mach 5 and 30 km altitude, and land start point: $M=0.294$ and $h=10$ m end point: $M=0.35$ and $h=500$ m			
vehicle configuration	100% reusable			
propulsion system	turbojet-ramjet			
objective function	minimize time			
constraints	-turbojet at 100% throttle cannot exceed Mach 3 (CIT limit = 470 K) -vehicle structure cannot exceed Mach 5 -dynamic pressure cannot exceed 62 kPa ($q < 9$ psi) -horizontal acceleration $-3.5g < a_x < 3.5g$ -vertical acceleration $-1.5g < a_z < 1.5g$ -vehicle rotation $-5 < \dot{\gamma} < 5$ deg/s -aircraft trimmed to have zero longitudinal moment			
Analysis tool	Dymos / OpenMDAO			
Solver specifications	Radau collocation; IPOPT driver			

2. Problem Description

2.1. Mission Objective

The Hello-1X (H1X) vehicle shown in Fig. 1 is a 100% reusable horizontal takeoff and landing aircraft with a turbojet-ramjet propulsion system. It is being developed by Space Engine Systems as a piloted demonstrator vehicle with an unmanned option in advance of their two-stage-to-orbit Hello-1 spacecraft that is capable of delivering a 550 kg payload to 600 km sun-synchronous orbit whose preliminary trajectory result is available in [16]. The expected peak operational capability for H1X is Mach 5 at 28–32 km altitude. Table 1 outlines the trajectory study evaluated in this paper. (Mach numbers mentioned in this paper are evaluated at the local height-dependent ambient temperature.) The chosen start and end points were a consequence of not having data available that factors in the ground effect or extended landing gear.

The trajectory consists of five propulsion phases: turbojet (TJ), mixed (mix=TJ+RJ), ramjet (RJ), glide (GD), and powered descent (PL). The first three phases occurred during ascent to the mission objective defined for this paper as M=5 at h=30 km. The TJ and mix phases set the TJ to 100% throttle

with after-burner (AB) engaged. Fuel injected into the RJ was limited by the RJ throat area for M<4and equivalence ratio ER=0.9 thereafter. Descent includes a GD phase where the amount of fuel added into the RJ is dictated by the compressor inlet temperature (CIT) limit and PL phase where fuel is injected into the turbine combustor and the TJ could be throttled. The trajectory analyzed in this effort was optimized using a minimum time objective. Consumed fuel is reported to inform operating costs.

2.2. Trajectory Model

The Dymos [18] optimal control of dynamic multidisciplinary systems library built onto the OpenM-DAO [19] high-performance computing platform was utilized to simulate flight trajectories. An implicit time integration scheme was used to solve the governing equations of motion. The IPOPT driver [20] dealt with the NLP and the Radau pseudospectral collocation technique [21] was selected to iterate the trajectory. Several of the default driver settings were changed and listed in Table 2. A convergence check between the opt and sim solutions had goodness of fits (r2 scores) in excess of 0.99 for each phase where the driver declared convergence prior to the iteration limit for successful simulations. Code outputs include height h, range r, and vehicle mass m as functions of time t. To ensure continuity between phases, linkage constraints were specified for time, state, and control variables. Optimizations were performed on one core of an AMD Ryzen[™] 9 5900X 12-core processor with 64 GB RAM. It was invaluable to check partials during code debugging.

-			
Parameter	Value	Parameter	Value
max_iter	150	adaptive_mu_globalization	kkt-error
tol	10^{-5}	alpha_for_y	safer-min-dual-infeas
dual_inf_tol	10^{-4}	linear_solver	mumps
constr_viol_tol	10^{-7}	required_infeasibility_reduction	0.99
bound_mult_init_method	mu-based	hessian_approximation	limited-memory
nlp_scaling_method	gradient-based	limited_memory_max_history	100
mu_min	10^{-13}	limited_memory_max_skipping	5

Table 2. IPOPT parameters.

Figure 2 is a free-body diagram showing the relevant forces acting on an aircraft. The direction of motion along the thrust vector, which is angled relative to horizontal as the summation of angle-of-attack α and flight path γ angles. Balancing the aircraft weight was evaluated as a combination of vehicle lift and thrust. The governing equations are

$$\frac{dr}{dt} = v\cos(\gamma) \tag{1}$$

$$\frac{dh}{dt} = v \sin(\gamma) \tag{2}$$

$$\frac{dv}{dt} = \frac{T\cos(\alpha) - D - mg\sin(\gamma)}{m} \tag{3}$$

$$\frac{d\gamma}{dt} = \frac{T\sin(\alpha) + L - mg\cos(\gamma)}{mv} \tag{4}$$

and can be reduced to

$$C_{T} = \frac{W_{tot,t} \sin \gamma}{\cos \alpha \ qS} + \frac{C_{D}}{\cos \alpha}$$

$$C_{L} = \frac{W_{tot,t} \cos \gamma}{qS} - C_{T} \sin \alpha$$
(5)

$$C_L = \frac{W_{tot,t}\cos\gamma}{qS} - C_T\sin\alpha \tag{6}$$

for quasi-steady flight where $mq = W_{tot,t}$ is the total vehicle weight at time t, q is the dynamic pressure, and S is the reference aerodynamic area. The coefficients were input into Dymos using a one-way decoupled approach.

An informal grid convergence study was conducted where the number of segments discretizing the time histories of each phase are listed in Table 3 along with a summary of results at the RJ and PL phase end points. Weighting of the segment ends were specified using Legendre-Gauss-Lobatto nodes. Although there is a more appreciable change between the fine-medium solutions than the medium-coarse solutions to indicate that monotonic convergence has not been obtained and would yield larger uncertainties, the relatively small deltas between solutions gives confidence that the values are representative of a solution with increased refinement. Simulation attempts with additional refinement were unsuccessful as a consequence of a RAM limitation. The medium grid solution is shown in the results section.

	Grid	coarse	medium	fine	extra-fine
	num_segs [TJ,mix,RJ,GD,PL]	[4,8,8,8,8]	[6,12,12,12,12]	[9,18,18,18,18]	[9,18,22,22,22]
	solver time, s	208	430	1198	1881
	<i>t,</i> s	431	435	408	435
Þ	r, km	362	371	332	370
RJ end	γ , deg	0.8	0.6	1.0	0.0
24	$m_{jetA}/m_{tot,0}$	0.0247	0.0246	0.0246	0.0246
	$m_{H2}/m_{tot,0}$	0.0790	0.0817	0.0742	0.0776
	<i>t,</i> s	890	872	834	849
	r, km	708	697	651	676
	γ , deg	0.0	0.1	0.0	0.0
	$m_{jetA}/m_{tot,0}$	0.0304	0.0302	0.0302	0.0300
	$m_{H2}/m_{tot,0}$	0.0835	0.0858	0.0782	0.0814

Table 3. Grid study.

2.3. Trimming Module

A trimming module was developed to balance the longitudinal moments by deflecting the elevator. An approach similar to that described in Hermann, Cox, and Mavris [6] was created. The module was specified as an implicit component where inputs included the thrust, drag, and moment contributions C_m for the aircraft less the elevator surfaces at α plus the moment contribution of the elevator at δ , $C_{m.elev}$:

$$C_m(\alpha) + C_{m,elev}(\delta) - C_{m,elev}(\alpha) = 0$$
(7)

A nonlinear function was specified to solve the δ residual. Newton's solver was specified to solve the implicit function where the BoundsEnforceLS method was specified for the linesearch and the DirectSolver for the linear solver.

2.4. Parameter Database

Figure 3 shows a schematic that distinguishes which components were considered to quantify lift and drag from CFD, or thrust and fuel rates using pyCycle. The decision to specify the inlet interface within the duct was a consequence of asymmetric forces acting on the 2D inlet internal compression surfaces that had an appreciable impact on lift whereas the nozzle interface was specified at the respective TJ and RJ throats as a consequence of the SERN configuration where it was impractical to resolve a surface at the projected nozzle outlet in the CFD model. Calculation of standard thrust, specific impulse and vehicle L/D, however, required projected values at the nozzle outlets.

Static longitudinal moments were calculated around a centre-of-gravity (CG) that was allowed to vary between CGdry and CGwet as a function of the remaining fuel where the H2 tank was positioned in the front-half of the vehicle and jetA tanks adjacent to the TJ.

2.4.1. Aerodynamic Inputs

Steady-state fully turbulent 3D solutions with the Reynolds-Averaged Navier-Stokes equations were obtained using the commercially available CFD code Siemens STAR-CCM+© version 2402 [22]. It is

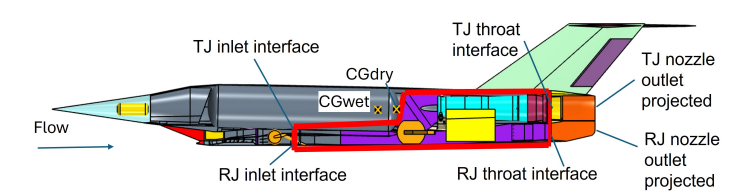


Fig 3. Bookkeeping schematic. Inside red box: thrust coefficient calculated from PyCycle. External to red box: lift and drag coefficients obtained from CFD.

not strictly accurate to assume steady-state given the accelerating flight path; however, at instants in-time, the aerodynamic coefficients are quasi-steady. Turbulence was quantified using the shear stress transport (SST) model [23]. Following the recommendation in [24] and [25], a1=0.355, the compressibility correction was disabled, and the QCR constitutive option was selected.

Using the same setup as described in [16], the equation set for the fluid domain was solved using the Coupled flow model with implicit integration where derivatives were discretized using the MUSCL 3rd-order central-differencing scheme with inviscid flux equated using AUSM+ flux-vector splitting [26] and incomplete lower-upper relaxation [27]. The AMG linear solver had a convergence tolerance of 0.01 and used the F cycle with 2 post-sweeps and bi-conjugate gradient stabilized acceleration. Radiation transfer in simulations with M>2 was accounted for using the surface-to-surface radiation model assuming wavelength-independent properties via the Gray Thermal spectrum model where Kirchhoff's law was enforced at the surfaces. View factors were calculated using 1024 beams between the surfaces and the surroundings. Solar radiation was neglected.

Solutions were initialized using grid sequencing. For conditions with M>1, a sub-region was constructed around the internal duct with a subsonic velocity to ensure that the domain outlet boundary downstream of the inlet isolator had subsonic flow whereas the external regions assumed freestream conditions. Iterations proceeded using the automatic CFL control that was allowed to vary 0.1 < CFL < 50 with the line search option allowing explicit relaxation to vary between 0.1 and 0.3. Farfield domains assumed 100% air; however, to better match the exhaust massflow and temperature between CFD and pyCycle, exhaust inlet boundaries were specified as a combination of air and water vapour. Fluids were evaluated as ideal gases where specific heat capacity, viscosity and conductivity were expressed as functions of temperature. Ambient conditions were obtained from Python's ambiance package [28].

Figures 4(a) and 4(b) show sample lift and drag forces acting on the H1X vehicle obtained at a supersonic flight condition. Negative lift values on the top surfaces shown are beneficial whereas positive drag forces

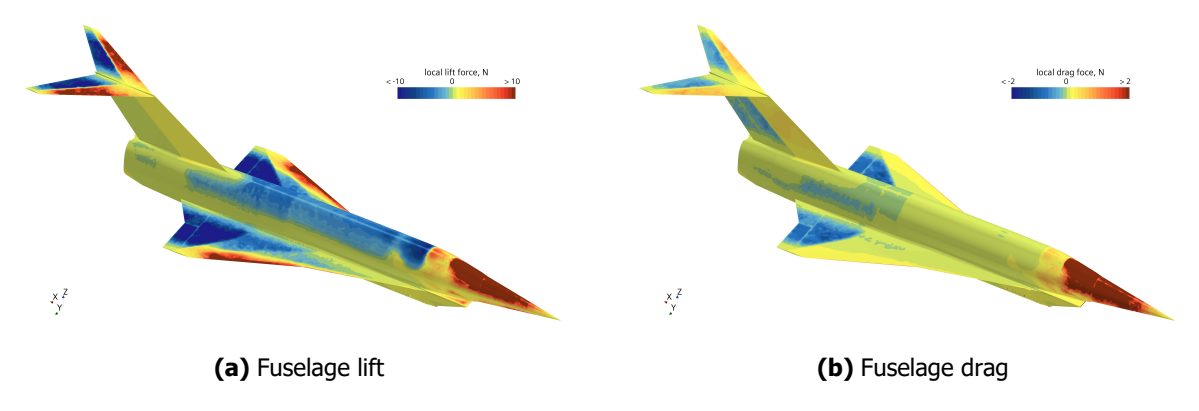


Fig 4. Sample CFD solution at a supersonic velocity showing local forces acting on the Hello-1X demonstrator vehicle.

on forward-facing surfaces and negative values on rear-facing surfaces are detrimental. It is apparent that the nosecone has a significant contribution to poor loading performance and that lifting surfaces must be designed as a compromise between lift and drag needs. Detailed component CFD analyses of the inlet, precooler, RJ combustor, nozzle, and wing are available by the authors in [29], [11], [30], [31], and [32] respectively.

2.4.2. Engine Cycle Inputs

pyCycle, a thermodynamic cycle modeling library built on top of the OpenMDAO framework [33] generated a database of thrust coefficients and fuel consumption rates for the airbreathing engines. The library was developed to identify more efficient design methods for unconventional aircraft and propulsion concepts with the capability of being a module integrated within a larger multidisciplinary optimization process [33]. The use-case in this study was a decoupled one-way passing of the engine performance parameters into Dymos. Analytic derivatives were used where possible to improve accuracy and computational efficiency in the gradient-based optimization.

The same engine code that was leveraged by [16] was used to generate results for this study. In brief, modelling the TJ system made use of compressor, combustor, and turbine elements that required input maps for parameters including pressure ratio, flow rate, and efficiency. Additionally, elements for an inlet, precooler, and nozzle were added to the TJ flowpath that received loss estimates from CFD. Using a similar modular approach, the RJ flowpath was built using inlet, duct, combustor, and nozzle elements. pyCycle stitched the elements together to form a model for the engine architecture where thermodynamic property and/or engineering calculations are completed. Within an element, tasks including applying a pressure ratio to the inlet value or calculating the heat from a chemical reaction to determine the exit value [33]. In doing so, the code outputs thermodynamic solutions at the defined stages.

It was assumed that the TJ would burn liquid hydrocarbon fuel (jetA) and RJ would run on hydrogen. In addition to H2-air having higher specific impulse, carrying liquid H2 acts as the TJ precooler energy sink in order to extend operation to Mach 3 for engines available in the market without having to modify the compressor blade material.

2.5. Initial Guess

Determining an initial ascent trajectory leveraged viewing the input data in Figs. 5(a) and 5(b), showing contours of specific excess thrust

$$SET = \frac{T - D}{W_{tot}} \tag{8}$$

and specific excess power

$$SEP = \frac{T - D}{W_{tot}}v\tag{9}$$

on M vs. α and M vs. h grids respectively. The SET plot includes lines showing where lift equals initial weight at h=0 m and q=9 psi to identify the lower bounds of possible flight and thrust = drag to identify the upper bound of operation. Positive thrust at $\alpha=0$ deg gives confidence that a solution is feasible to M=5 and at least h=23 km (q=9 psi) without requiring data manipulation. Mach 5 and h=30 km coincides with q=3 psi dynamic pressure: the 3 psi line drawn on the plot shows that there is insufficient thrust between 3 < M < 3.5 and at M=5 suggesting that performance enhancements are necessary to achieve higher altitudes at M=5.

The positive SEP values in Fig. 5(b) indicate the opportunity for the aircraft to increase potential energy or kinetic energy. The deficits at $M\approx 1$. and 3< M<3.5 coincide with TJ drop-offs due to higher spillage drag penalties with increasing velocity and throttling down respectively. Maximum SEP is shown at M=3 where TJ and RJ are both at peak performance and at $M\approx 4.5$ where RJ I_{sp} reduction with velocity and reduced inlet spillage drag given a more favourably sized capture area are competing factors. Energy height lines identify where an altitude decrease is balanced by a velocity increase. Dynamic pressure q contours are drawn since a constant dynamic pressure trajectory is considered to be an acceptable compromise between structural loading and engine performance. Flying at constant

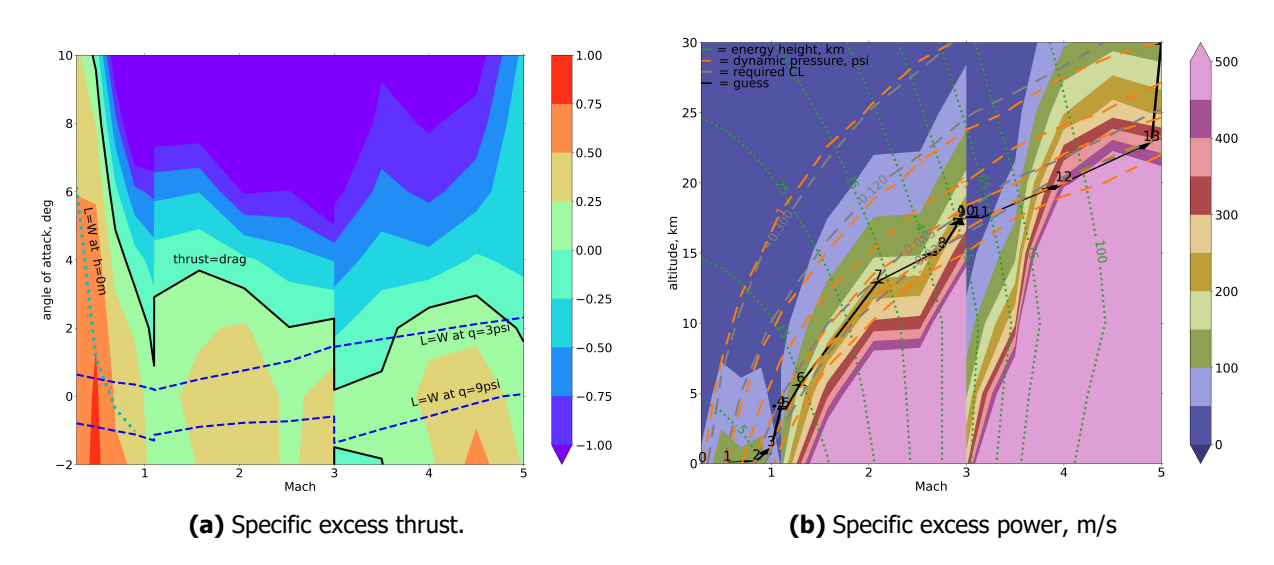


Fig 5. Input data

q may also alleviate some wing and trimming design challenges given that C_L remains approximately constant.

Points for the initial guess were visually placed on Fig. 5(b) to coincide with the q limit. Pull-up manoeuvres were specified at the TJ-mix and mix-RJ transitions and it was found from initial trajectory attempts that a zoom climb to the h=30 km altitude objective at the maximum velocity was beneficial for reducing mission time. Time durations were evaluated based on the average vertical velocity components and ranges were calculated from time and the average horizontal velocity component. The initial descent trajectory was linearly interpolated from the end points where it was assumed that the GD-PL transition occurred at M=2 and h=11.4 km.

2.6. Constraints

Table 4 lists the bounds for the state and control variables. Additionally, path constraints were defined for h, M, $q < 9 \mathrm{psi}$, $-15 < a_z < 15 \mathrm{m/s^2}$, and $-5 < \dot{\gamma} < 5 \mathrm{deg/s}$. Whereas bounds for h, r, m, and γ were specified for completeness, α bounds were cognizant of performance impact to lift and drag. Relatively tight t bounds were specified to minimize the solver search space. Duration bounds were modified as-needed if solution infeasibility was a consequence of the selected limits.

Phase	ТЈ	mix	RJ	GD	PL
duration t , s	[50,180]	[100,450]	[50,580]	[150,500]	[150,400]
altitude h , km	[0.01,8.]	[0.01,30]	[10,40]	[1,40]	[0.45,20]
velocity v , m/s	[90,535]	[320,895]	[797,1540]	[578,1540]	[113,602]
Angle of attack α , deg	[-5,10]	[-4, 5]	[-4, 5]	[-10,10]	[-20,20]
Flight path angle γ , deg	[-85,85]	[-60,60]	[-10,40]	[-80,40]	[-40,40]

Table 4. State variable bounds.

3. Results

Figure 6 shows trajectory height vs. range and height vs. Mach solutions for the ascent and descent components of the mission whereas Fig. 7 shows select trajectory metrics vs. time. During the TJ phase, the vehicle quickly accelerates to $M\approx 1$ and then rapidly ascends to h=4 km. A modest pull-up and dive manoeuvre occurs at the M=1.1 TJ-mix transition where fuel starts to be added to the RJ duct; the altitude change can be seen by the slight dip in q and α . The mix phase predominantly follows a

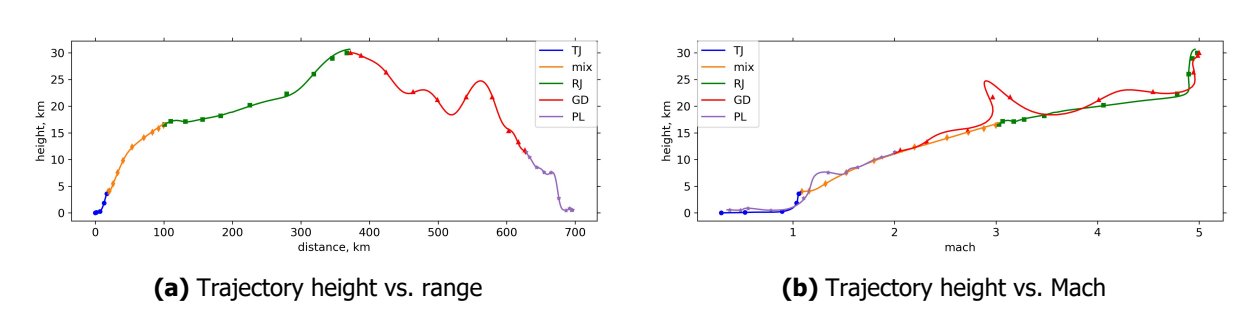


Fig 6. Trajectory outcomes. Phases: blue circles=TJ, orange diamonds=mix, green squares=RJ, red triangles=GD, purple stars=PL. lines=simulated solution, symbols=optimized solution.

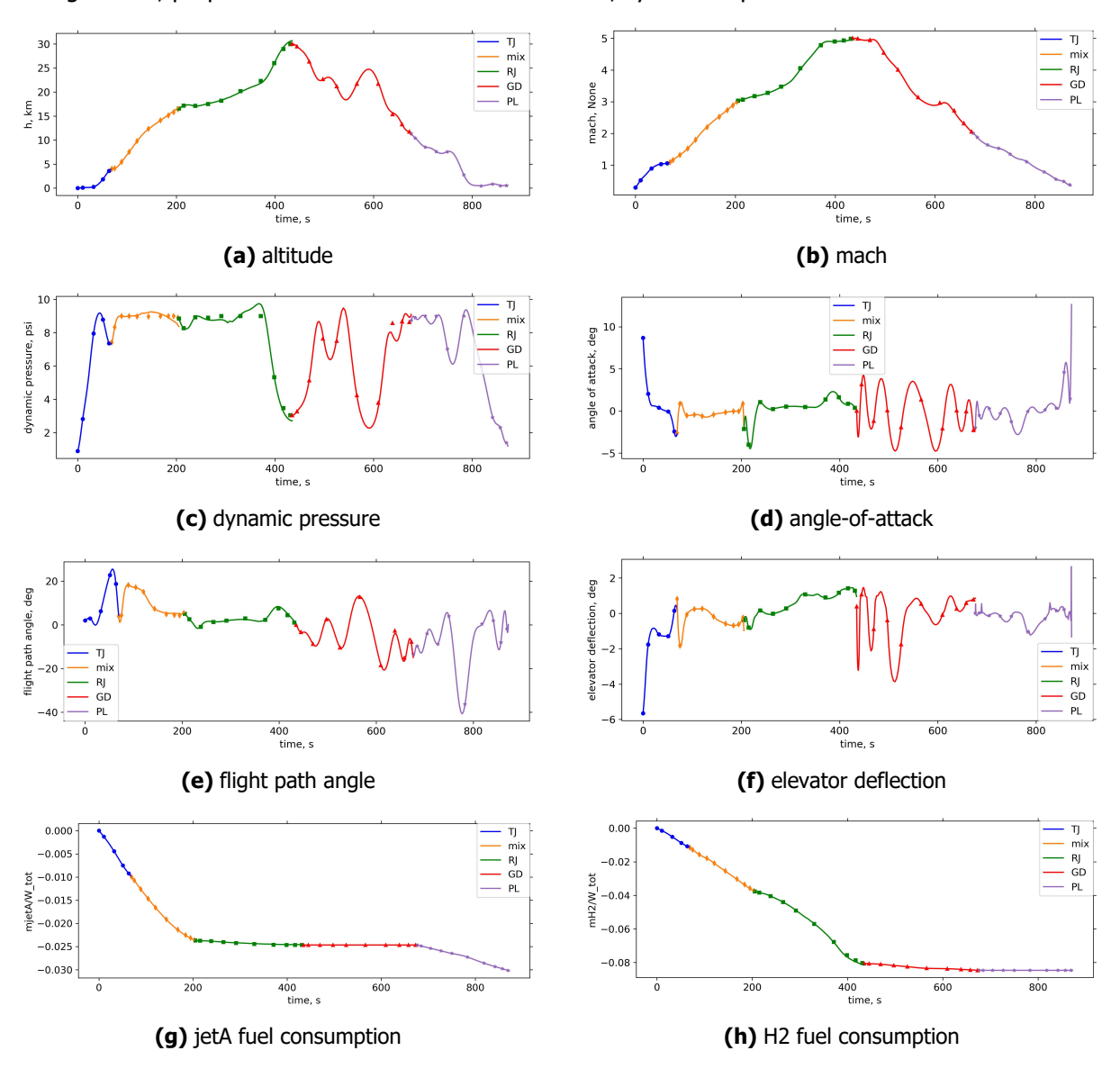


Fig 7. Trajectory metrics vs. time for M=5 at h=30km mission objective. Thrust factors [TJ,mix,RJ,GD,PL] = [1.1,1.15,1.2,0.3,0.3].

q=9 psi trajectory with $\alpha\approx-0.5$ deg. Another pull-up and dive manoeuvre occurs at the M=3 mix-RJ transition followed by RJ flight predominantly at q=9psi with $\alpha\approx0.5$ deg. To reach the altitude goal, zoom-up to h=30km occurs at $M\approx5$. At the RJ-GD transition, the optimizer selected $\alpha=0$ deg and $\gamma=0.6$ deg.

The α increase in the RJ phase is consistent with the SR-71 inlet orientation that suggests the aircraft is flying at positive angle-of-attack at its maximum Mach. Although not investigated since the flight envelope q constraint impacted the result, it is suspected that there is a preference for accelerating supersonic trajectories to occur at constant q since C_L is approximately constant with M and the wing design point was at $\alpha=0$ deg.

During descent, the trajectory is appreciably oscillatory due to alternating reductions in potential energy and kinetic energy. These manoeuvres were characterized as 'S-turns' in the Space Shuttle's re-entry plan to operate at high α to maximize drag and dissipate speed [34]. Rapid potential energy reductions are capped by the q and a_z constraints where a_z is more appreciably influenced by $\dot{\gamma}$. The GD-PL transition occurs at M=2, h=11km, and $\gamma=-15$ deg and the trajectory ends with $\gamma=0$ deg. The range covered during ascent is 371 km in 435s and 326 km distance is travelled in 438s during descent.

Figure 7(g) shows that jetA fuel is consumed during the TJ, mix, and PL phases whereas Fig 7(h) shows that H2 fuel is consumed in the AB during the TJ and mix phases, and RJ combustor in the mix, RJ, and GD phases. Although the requirement to consume H2 during GD is more appreciably influenced by the CIT limit, the nominal thrust is helpful in respecting the acceleration constraints. This analysis shows that the amount of fuel needed to complete this mission is 11.6% of the take-off mass. Not considered is the amount of jetA that the turbine would consume during cooldown after it is throttled down at M=3 or quantities needed for take-off and landing, which is estimated to be an additional 1%.

Figure 8(a) shows specific impulse

$$I_{sp} = \frac{F_{n,TJ} + F_{n,RJ}}{(\dot{m}_{jetA} + \dot{m}_{H2}) g}$$
 (10)

histories given standard thrust

$$F_n = \dot{m}_e v_e - \dot{m}_0 v_0 + A_e \left(p_e - p_0 \right) \tag{11}$$

for 0=freestream values at the capture area and e=projected nozzle outlet. The magnitude and decrease during the TJ phase is characteristic for a hydrocarbon fuel. The increase during the mix phase happens because of the increasing amount of heat added into the RJ duct. Peaks in the TJ and mix phases are attributed to altitude changes. The first half of the RJ phase is negatively impacted by additional H2 needed by the precooler for the air going through the TJ whereas the flow rate through the TJ drops off beyond M>3.5. Figure 8(b) confirms that a step change occurs in SET at $M\approx3.5$. The GD and PL phases have positive I_{sp} due to precooler needs in GD and turbojet operation in PL. The values may seem artificially high due to the relatively small fuel flow rates where Fig.8(b) shows that the vehicle is primarily decelerating in these phases.

Figure 8(c) plots static margin

$$K_n = -\frac{dC_m}{d\alpha} / \frac{dC_N}{d\alpha} \tag{12}$$

where \mathcal{C}_m included the thrust contributions to longitudinal moment and

$$C_N = C_L \cos \alpha + C_D \sin \alpha \tag{13}$$

The derivatives were calculated using a first-order backwards differencing approximation where C_m and C_N were evaluated at $\alpha-1$ deg. This reduced-order method is responsible for the noise seen at the start of the RJ phase. The trends follow expectations that K_n decreases with velocity. Although $K_n>0.05$ is suggested for supersonic aircraft as a minimum distance for the neutral point to be positioned behind the centre of gravity [35], the fact that $K_n>0$ throughout is encouraging for mission viability. Furthermore,

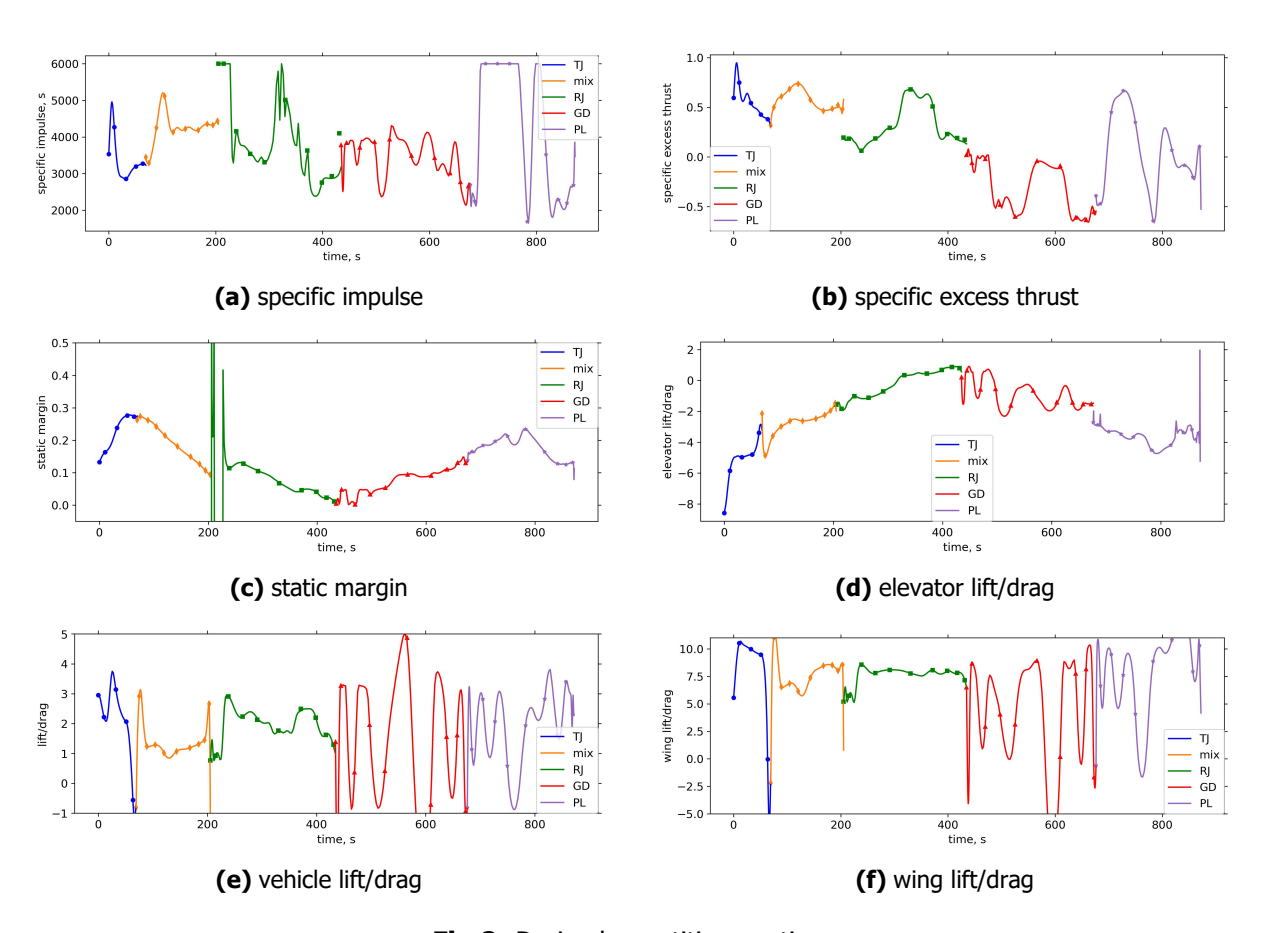


Fig 8. Derived quantities vs. time

Fig. 7(f) shows that the elevator has a relatively small deflection range to maintain longitudinal static stability, suggesting that the lifting surface positions and control surface sizes are adequate. Having said that, Fig. 8(d) shows that the elevator predominantly creates negative lift whose impact could be reduced by reducing the pitch-down moment created by the SERN nozzle.

Figures 8(e) and 8(f) show overall vehicle lift-to=drag ratio and wing lift-to-drag ratio. Low vehicle L/D values are attributed to including the internal compression region of the inlet in the calculation where there are appreciable asymmetric forces acting on the top- and bottom surfaces. In comparison the wing $L/D \approx 8$ during ascent is more aligned with performance expectations for supersonic delta wings with diamond-shaped airfoils.

Table 5 summarizes the key trajectory metrics showing a mission duration of 872 s and total range of 697 km. The final column in the table quantifies enhancement factors during the various phases of flight that were required in order to obtain a feasible result. The factors in the TJ, mix, and RJ phases were applied to thrust without influencing fuel consumption and could equivalently be interpreted as drag reductions. The factors applied to the GD and PL phases throttled both thrust and fuel.

3.1. Discussion

Kaneko and Martins [4] advised that generating a good initial guess is crucial for solving complex optimization problems both for computational efficiency and robustness. A three-step procedure was introduced that included extensive trial and error of the initial guesses, scaling, and optimization options; inequality constraint relaxation; and reducing the problem size by removing physical system design variables with the caution that the additional degrees of freedom may allow the optimizer to navigate through infeasible regions.

Table 5. Trajectory medium-grid solution summary. Factors for TJ, mix, and RJ identify performance enhancements needed without increasing fuel consumption whereas the GD and PL factors throttle both thrust and fuel.

Point	Mach	height, km	range, km,	duration, s	jetA fuel	H2 fuel	factor
start	0.29	0.01	0	0	0	0	_
TJ end	1.1	4.0	18.6	69	0.010	0.012	1.1
mix end	3.0	16.9	101.5	136	0.014	0.026	1.15
RJ end	5.0	30.7	371.2	229	0.001	0.044	1.2
GD end	2.0	11.1	627.7	242	0	0.004	0.3
PL end	0.35	0.57	696.9	196	0.006	0	0.3
total				872	0.030	0.086	

Following this procedure helped to mitigate setup-induced failures and clarify which actions have positive impact. In particular, leaving the thrust factors as one resulted in the non-feasible outcome shown in Fig. 9 where solutions could not be found in the RJ and PL phases despite tripling the duration bounds. The plots show the failure since the optimized result obtained from IPOPT does not match the simulated result that uses a numerical integrator to verify that the governing equations are solved correctly. Whereas the TJ can be throttled to reduce thrust to achieve the set height and velocity at the PL end, the inability to achieve the altitude objective is consistent with the performance deficiency highlighted in Fig. 5(a) at M=5.

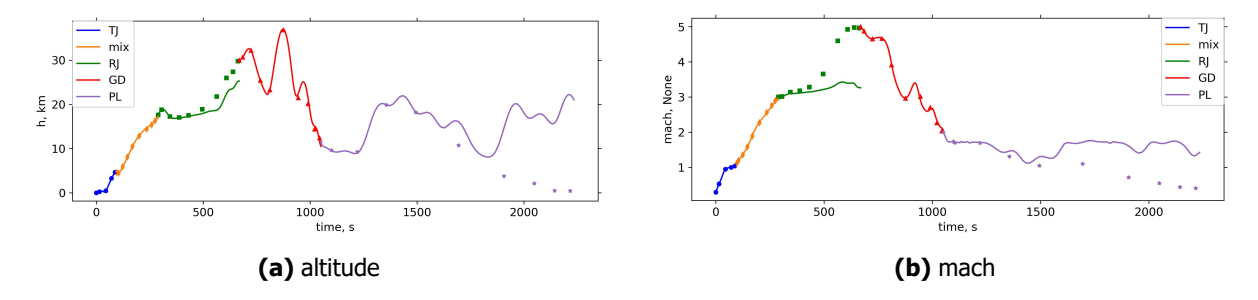


Fig 9. Failed solution with M=5 at $h=30 \mathrm{km}$ mission objective. Thrust factors [TJ,mix,RJ,GD,PL] = [1,1,1,1,1].

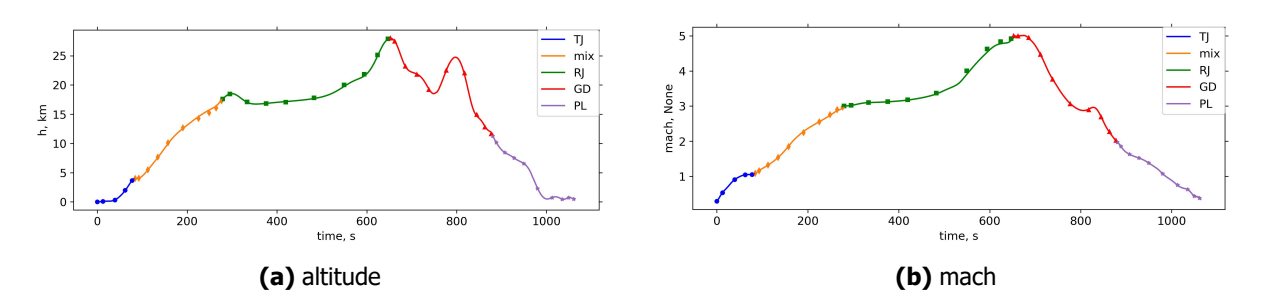


Fig 10. Viable solution not requiring thrust enhancement with M=5 at h=28km mission objective. Thrust factors [TJ,mix,RJ,GD,PL] = [1,1,1,0.3,0.3].

To confirm that the infeasibility was a consequence of the available performance within the flight envelope of the RJ phase, Fig. 10 shows a converged trajectory solution with a M=5 at h=28km altitude

height objective	h = 30 km	h = 30 km	$h=28~\mathrm{km}$	
factors	[1.1,1.15,1.2,0.3,0.3]	[1.,1.,1.,1.]	[1.,1.,1.,0.3,0.3]	
driver exit reason	exit reason optimal solution found max iterations exceeded		optimal solution found	
trajectory solution	Fig. 7	Fig. 9	Fig. 10	
primal infeasibility	5.3e-8	9.3e-2	4.2e-6	
dual infeasibility	1.6e-7	4.0e1	1. 4 e-6	
constraint violation	5.3e-8	9.3e-2	4.2e-6	
variable bound violation	0.	0.	0.	
complementarity	8.0e-7	3.0e-2	8.0e-7	

Table 6. IPOPT final metrics.

mission objective. Maximum α in the RJ phase for M>4.5 was $\alpha=2$ deg whereas $\alpha=2.5$ deg is seen in Fig. 7(d) to reach h=30km. Although the failed solution in Fig. 9 showed successful convergence of the GD phase with thrust factor=1, it was elected to produce this h=28km solution with factor=0.3 during descent to decrease mission duration. In the event that the H2 flow rate is driven by the precooler requirement, a drag enhancement degree-of-freedom can be added to the model to offset the thrust generated by the RJ. Goodness of fits in all phases were above 0.99. Fuel fractions were 0.041 jetA and 0.12 H2.

Examining the IPOPT.out file assisted efforts in diagnosing trajectory convergence difficulties whose final metrics are summarized in Table 6. Primal infeasibility is caused by conflicting constraints, a poor initial guess, an over-constrained system, or numerical issues. Dual infeasibility assesses the optimality of the solution and how closely the constraints are satisfied. Constraint violation reports the maximum absolute constraint residual. Variable bound violation refers to how much the solution violates the specified upper and lower bounds. And complementarity refers to how well the solution satisfies the complementarity conditions such as Lagrange multipliers of the Karush-Kuhn-Tucker (KKT) system [36, 37]. Whereas the $h=30{\rm km}$ solution with factors and $h=28{\rm km}$ solution achieved errors below the assigned tolerances, the $h=30{\rm km}$ outcome with factors=1 errors substantiated that a solution using un-modified input coefficients that respects the constraints does not exist.

4. Conclusions

Generating specific excess thrust and specific excess power plots from the input coefficients was instrumental in identifying a possible flight envelope and defining an initial guess for the trajectory. By utilizing a throttle degree-of-freedom, a solution with a M=5 at h=30km mission objective for a supersonic aircraft with a turbojet-ramjet combined-cycle with 5 propulsion phases distinguished for ascent and descent was found. Reviewing the constraint summary metrics from the IPOPT driver output helped to clarify feasibility challenges. Removing the throttle factor from the ascent phases restricted the mission altitude to 28km; the trajectory obtained $\alpha < 2$ deg for M > 4.5, which agreed with the maximum allowable α for thrust=drag seen on the specific excess thrust plot.

For the Mach 5 at 30km altitude mission, it took 435s for ascent and 438s for descent, travelling a total of 672 km and consuming 3% jetA and 8.6% H2 of the initial vehicle mass. Noteworthy features of the mission included preference to fly at approximately zero angle-of-attack and 9psi dynamic pressure with pull-up manoeuvres at phase transitions. The vehicle was trimmed via an elevator deflection range between -6 and 1 deg and static longitudinal stability occurred throughout.

References

- [1] Forbes-Spyratos, S., "Trajectory Optimisation of a Partially-Reusable Rocket-Scramjet-Rocket Small Satellite Launch System," Ph.D. thesis, The University of Queensland, 2020. https://doi.org/10.14264/31e3e84.
- [2] Mehta, U., Bowles, J., Melton, J., Huynh, L., and Hagseth, P., "Water injection pre-compressor cooling assist

- space access," The Aeronautical Journal, Vol. 119, No. 1212, 2015, pp. 145–171. https://doi.org/10.1017/S0001924000010319.
- [3] Lock, A., Oberman, G., Jahn, I. H., van der Heide, C., Bone, V., Dower, P. M., and Manzie, C., "Hypersonic glide vehicle shape and trajectory co-design," AIAA SCITECH 2025 Forum, 2025, p. 1337. https://doi.org/ 10.2514/6.2025-1337.
- [4] Kaneko, S., and Martins, J. R., "Simultaneous design and trajectory optimization strategies for computationally expensive models," *AIAA Journal*, Vol. 63, No. 2, 2025, pp. 420–438. https://doi.org/10.2514/1.J063976.
- [5] van der Heide, C., Cudmore, P., Jahn, I., Bone, V., Dower, P. M., and Manzie, C., "Feasibility detection for nested codesign of hypersonic vehicles," 2023 62nd IEEE Conference on Decision and Control (CDC), IEEE, 2023, pp. 632–637. https://doi.org/10.1109/CDC49753.2023.10384006.
- [6] Herrmann, E. G., Cox, A., and Mavris, D., "Multidisciplinary Design and Analysis of a Hypersonic Glide Vehicle With Trimmed Aerodynamics," AIAA SCITECH 2025 Forum, 2025, p. 1338. https://doi.org/10.2514/6.2025-1338.
- [7] Taguchi, H., Futamura, H., Yanagi, R., and Maita, M., "Analytical study of pre-cooled turbojet engine for TSTO Spaceplane," 10th AIAA/NAL-NASDA-ISAS International Space Planes and Hypersonic Systems and Technologies Conference, 2001, p. 1838. https://doi.org/10.2514/6.2001-1838.
- [8] Taguchi, H., Kobayashi, H., Kojima, T., Ueno, A., Imamura, S., Hongoh, M., and Harada, K., "Research on hypersonic aircraft using pre-cooled turbojet engines," *Acta Astronautica*, Vol. 73, 2012, pp. 164–172. https://doi.org/10.1016/j.actaastro.2011.10.006.
- [9] Taguchi, H., Harada, K., Kobayashi, H., Hongoh, M., Masaki, D., and Nishida, S., "Mach 4 Simulating experiment of pre-cooled turbojet engine using liquid hydrogen," *Aerospace*, Vol. 9, No. 1, 2022, p. 39. https://doi.org/10.3390/aerospace9010039.
- [10] Cai, C., Zheng, Q., Fang, J., Chen, H., Chen, C., and Zhang, H., "Performance assessment for a novel supersonic turbine engine with variable geometry and fuel precooled: From feasibility, exergy, thermoeconomic perspectives," *Applied Thermal Engineering*, Vol. 225, 2023, p. 120227. https://doi.org/10.1016/j.applthermaleng.2023.120227.
- [11] Cerantola, D. J., Schmidt, G., Handford, D., and Dass, P., "TPMS Turbojet Precooler Design Methodology and Case Study," *Turbo Expo: Power for Land, Sea, and Air*, Vol. 88094, American Society of Mechanical Engineers, 2024, p. V013T13A009. https://doi.org/10.1115/GT2024-122645.
- [12] Hoopes, C., and Takahashi, T., "Lateral-Directional Controllability Impacts of Longitudinal Pitch Trim Strategies on the Space Shuttle Orbiter," *AIAA SCITECH 2024 Forum*, 2024, p. 2318. https://doi.org/10.2514/6.2024-2318.
- [13] OBrien, K., and Takahashi, T., "Tail Sizing Strategies to Ensure Low-Risk Maneuvering High-Speed Flight," AIAA SCITECH 2024 Forum, 2024, p. 2320. https://doi.org/10.2514/6.2024-2320.
- [14] Kabganian, M., Hashemi, S., and Roshanian, J., "Multidisciplinary Design Optimization of a Re-Entry Spacecraft via Radau Pseudospectral Method," *Applied Mechanics*, Vol. 3, No. 4, 2022, pp. 1176–1189. https://doi.org/10.3390/applmech3040067.
- [15] Herman, A., and Conway, B., "Direct optimization using collocation based on high-order Gauss-Lobatto quadrature rules," *Journal of Guidance, Control, and Dynamics*, Vol. 19, No. 3, 1996, pp. 592–599. https://doi.org/10.2514/3.21662.
- [16] Cerantola, D. J., Handford, D., and Dass, P., "Combined Air-Breathing and Rocket Propulsion System Trajectory Analysis for Delivering Payload to Space," 75th International Astronautical Congress, International Astronautical Federation, 2024, pp. IAC–24–C4.7.11,x90349. URL https://iafastro.directory/iac/paper/id/90349/summary/.
- [17] Falck, R., Gray, J., and Naylor, B., "Parallel aircraft trajectory optimization with analytic derivatives," 17th AIAA/ISSMO Multidisciplinary Analysis and Optimization Conference, 2016, p. 3207. https://doi.org/10.2514/ 6.2016-3207.
- [18] Falck, R., Gray, J., Ponnapalli, K., and Wright, T., "dymos: A Python package for optimal control of multidisciplinary systems," *Journal of Open Source Software*, Vol. 6, No. 59, 2021, p. 2809. https://doi.org/10.21105/joss.02809.

- [19] Gray, J., Hwang, J., Martins, J., Moore, K., and Naylor, B., "OpenMDAO: An open-source framework for multidisciplinary design, analysis, and optimization," *Structural and Multidisciplinary Optimization*, Vol. 59, No. 4, 2019, pp. 1075–1104. https://doi.org/10.1007/s00158-019-02211-z.
- [20] Kawajir, Y., Laird, C., and Wächter, A., "Introduction to Ipopt: A tutorial for downloading, installing, and using Ipopt, 2010," 2016. URL https://www.coin-or.org/svn/CoinBinary/CoinAll/stable/1.8/Installer/files/doc/Introduction%20to%20Ipopt.pdf.
- [21] Garg, D., Patterson, M., Darby, C., Francolin, C., Huntington, G., Hager, W., and Rao, A., "Direct trajectory optimization and costate estimation of general optimal control problems using a Radau pseudospectral method," AIAA guidance, navigation, and control conference, 2009, p. 5989. https://doi.org/10.2514/6.2009-5989.
- [22] Siemens Digital Industries Software, "Simcenter STAR-CCM+ User Guide v. 2402,", Siemens 2023. URL https://www.plm.automation.siemens.com/global/en/products/simcenter/STAR-CCM.html.
- [23] Menter, F. R., "Two-Equation Eddy-Viscosity Turbulence Model for Engineering Applications," AIAA Journal, Vol. 32, No. 8, 1994, pp. 1598–1605. https://doi.org/10.2514/3.12149.
- [24] Cross, P., and West, M., "Simulation of hypersonic flowfields using star-ccm+," Tech. rep., Naval Air Warfare Center Weapons Division, 2019. URL https://apps.dtic.mil/sti/pdfs/AD1069198.pdf.
- [25] Hoste, J. J. O. E., Piazza, B., and Miro-Miro, F., "A numerical study on supersonic intakes," *HiSST: 3rd International Conference on High-Speed Vehicle Science & Technology*, 2024, p. 025.
- [26] Liou, M.-S., "A sequel to AUSM: AUSM+," *Journal of computational Physics*, Vol. 129, No. 2, 1996, pp. 364–382. https://doi.org/10.1006/jcph.1996.0256.
- [27] Saad, Y., Iterative methods for sparse linear systems, Society for Industrial and Applied Mathematics, 2003.
- [28] Dettmann, A., ambiance, version 1.3.1, 2022. URL https://pypi.org/project/ambiance/, accessed May 25, 2023.
- [29] Cerantola, D. J., Handford, D., and Dass, P., "Take-Off to Mach 5 Ramjet Ramped Inlet Analytical Design Tool," AIAA SCITECH 2025 Forum, 2025, p. 0750. https://doi.org/10.2514/6.2025-0750.
- [30] Cerantola, D. J., Handford, D., and Dass, P., "Computational parametric study evaluating ramjet combustor geometry," *HiSST: 3rd International Conference on High-Speed Vehicle Science & Technology*, 2024, p. 252.
- [31] Cerantola, D. J., Gagnon, J., Handford, D., and Dass, P., "Design Methodology for Selecting a Single Expansion Ramp Nozzle Geometry that can Complete a Mission between Machs 3 and 7," 25th AIAA International Space Planes and Hypersonic Systems and Technologies Conference, 2023, p. 3052. https://doi.org/10.2514/6. 2023-3052.
- [32] Cerantola, D. J., Handford, D., and Dass, P., "Simulating Wing Thermal Loads at Supersonic Speeds," AIAA SCITECH 2024 Forum, 2024, p. 2295. https://doi.org/10.2514/6.2024-2295.
- [33] Hendricks, E., and Gray, J., "pyCycle: A Tool for Efficient Optimization of Gas Turbine Engine Cycles," *Aerospace*, Vol. 6, No. 87, 2019. https://doi.org/10.3390/aerospace6080087.
- [34] Benson, T., "National Aeronautics and Space Administration. Speed Regimes: Hypersonic Re-Entry,", 2021. URL https://www.grc.nasa.gov/www/BGH/hihyper.html, accessed September 13, 2024.
- [35] Seraj, S., and Martins, J. R., "Aerodynamic shape optimization of a supersonic transport considering low-speed stability," *AIAA Scitech 2022 Forum*, 2022, p. 2177. https://doi.org/10.2514/6.2022-2177.
- [36] Wächter, A., and Biegler, L. T., "On the implementation of an interior-point filter line-search algorithm for large-scale nonlinear programming," *Mathematical programming*, Vol. 106, No. 1, 2006, pp. 25–57. https://doi.org/10.1007/s10107-004-0559-y.
- [37] Kawajir, Y., Laird, C., Vigerske, S., and Wächter, A., "Ipopt Documentation,", 2021. URL https://coinor.github.io/Ipopt/index.html, accessed August 14, 2025.